Materials LAB

RESEARCH ARTICLE

Materials Lab 2025, 4, 250005

Hybrid perovskite/GaAs nanowire diodes

E.M. Darivianaki[1], M. Androulidaki[2,4], K. Tsagaraki[2,4], M. Kayambaki[2,4], G. Stavrinidis[2,4], G. Konstantinidis[2,4], E. Dimakis[3], N. T. Pelekanos[1,2] and C. C. Stoumpos[1*]

Halide perovskites have dominated the field of photovoltaics in the past decade with record-breaking efficiencies demonstrated very recently. Likewise, III-V semiconductors represent the state-of-the-art in photovoltaics, being the model system of photovoltaic structure engineering. Herein, we investigate the possibility of using GaAs as an Electron Transporting Layer (ETL), substituting conventional ETLs in halide perovskite photovoltaics. We demonstrate our hypothesis on hybrid $CH_3NH_3PbI_3$ perovskite/GaAs nanowire (NW) heterostructures, specifically choosing GaAs in its NW form to enhance the electrical contact area between the two materials. The thus obtained heterostructures exhibit a characteristic diode response with improved electrical characteristics when n-doped GaAs NWs are employed. These initial results, which are promising in terms of III-V/perovskite heterojunctions, can potentially lead to efficient $CH_3NH_3PbI_3$/GaAs NW photovoltaics.

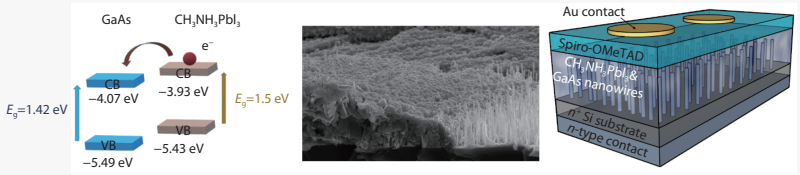

Perovskite solar cells have attracted great interest recently, and feature as one of the fastest developing technologies today in the field of photovoltaics[1]. Because of this, extensive studies were implemented on perovskite materials in the field of photovoltaics, developing various deposition techniques, targeting to improve the characteristics and the quality of perovskite materials that successfully resulted in a spectacular rise of solar cell efficiency and device stability as well[1-4]. The current trend involves the fabrication of tandem solar cell architectures, using a perovskite subcell in combination with other high-performance semiconductors to obtain exceptionally-high power conversion efficiency (PCE). The record efficiency for tandem solar cells up to date is 34.6% for a 2-terminal perovskite/silicon tandem solar cell device[5].

An attractive, yet, underestimated branch of tandem solar cells is the blend of perovskites with the other major player of photovoltaics (in terms of device performance), the III-V semiconductors and their key representative, GaAs[6,7]. GaAs is a model semiconductor with a large light absorption coefficient, a very high electron mobility value, good thermal stability, and a high refractive index[8,9,10,11]. In recent years, the development of GaAs photovoltaics turned into architectures based on GaAs NWs, as these structures present additional features due to their low dimensionality, including quantum confinement, anti-reflecting properties, enhanced light absorption and resonant wave-guiding effects[9,12-22].

Conceptually, GaAs is an excellent substitute to the regular TiO_2-based Electron Transporting Layers (ETLs), since it also has excellent band alignment in the conduction band relative to the perovskite (Fig. 1a) and, in addition, possesses a superior electron mobility, which is orders of magnitude higher than that of TiO_2[23,24].

As an initial step, to examine the potential of perovskite/III-V tandems, we fabricate $CH_3NH_3PbI_3$/GaAs NW heterostructures, in an architecture where n-doped GaAs NWs operate as an ETL, in order to evaluate the charge transport properties between the perovskite and GaAs NWs. In this configuration, we examine the behavior of the $CH_3NH_3PbI_3$ perovskite using an inverted n-i-p structure where we substitute the ubiquitous TiO_2 ETL layer with GaAs in its NW form.

Despite the fact that we have not been able to demonstrate direct photo-diode characteristics in the devices, we have been successful in demonstrating diode behavior from the $CH_3NH_3PbI_3$/GaAs NW heterojunction and to extract the basic diode characteristics.

Results and discussion

Fabrication of the heterostructure

The configuration of a typical hybrid perovskite/GaAs NW solar cell device consists of a p-i-n heterojuction, where GaAs NWs constitute the ETL layer (n-type material), enabling the

[1] *Department of Materials Science and Engineering, University of Crete, Heraklion 70013, Greece*

[2] *Microelectronics Research Group, IESL-FORTH, Heraklion 70013, Greece*

[3] *Institute of Ion Beam Physics and Materials Research, Helmholtz-Zentrum Dresden-Rossendorf, Dresden 01328, Germany*

[4] *Department of Physics, University of Crete, P.O. Box 2208, Heraklion 70013, Greece*

* Corresponding author, E-mail: cstoumpos@uoc.gr

Received 18 April 2025; Accepted 9 June 2025; Published online 9 June 2025

DOI: 10.54227/mlab.20250005

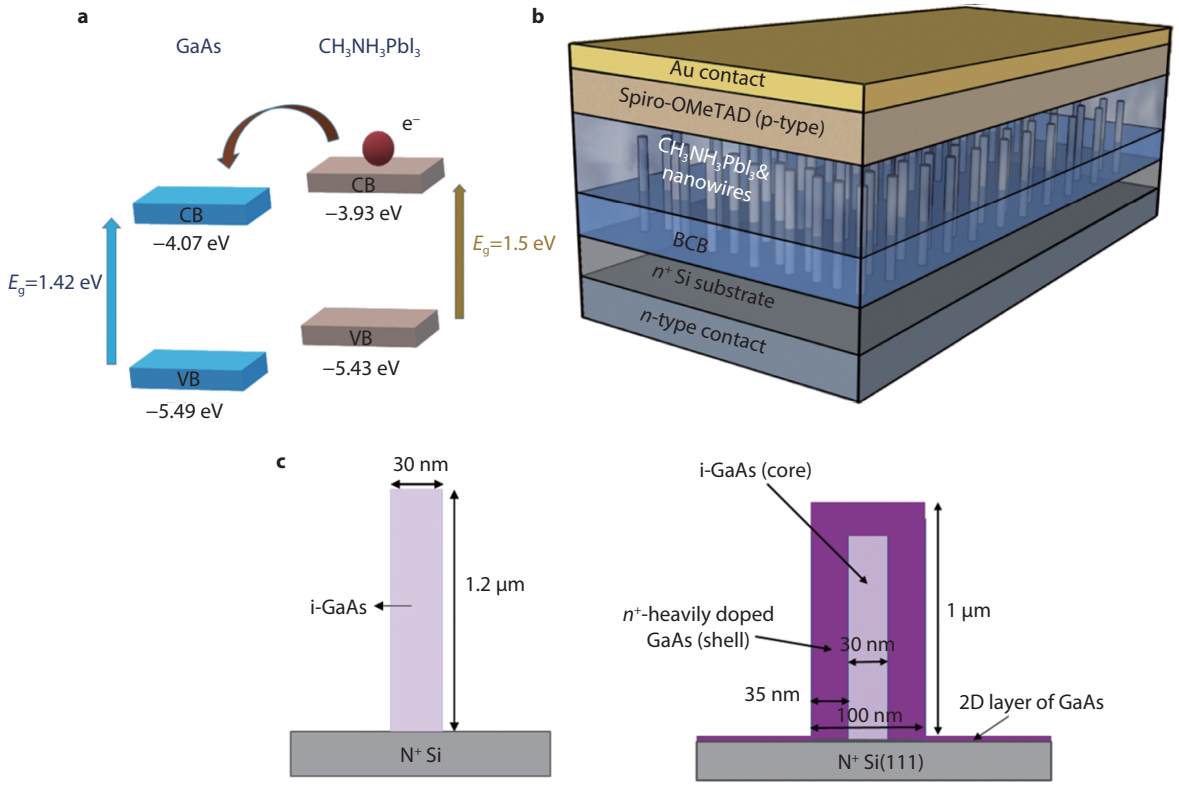

Fig. 1 **a** Schematic representation of energy levels for GaAs and $CH_3NH_3PbI_3$ perovskite, indicating favorable band alignment for electron transport between $CH_3NH_3PbI_3$ and GaAs. **b** The device architecture. **c** Schematic representation of the composition of the GaAs nanowires in intrinsic and doped variants, respectively. In the case of doped nanowires, a thin 2D layer of GaAs is also deposited on the substrate during the deposition of the GaAs shell.

extraction of photo-generated electrons. The $CH_3NH_3PbI_3$ perovskite is the photon absorbing layer (intrinsic material), while the hole transporting layer (HTL) (p-type material) consists of the perovskite-compatible triarylamine based molecule 2,2,7,7′-tetrakis-(N,N-di-p-methoxyphenylamine)9,9′-spirobifluorene (spiro-OMeTAD) and its documented doping cocktail. A thin-film of Au or a combination of Au with the transparent conducting oxide, Indium Tin Oxide (ITO) complete the electrical circuit. In this study, we deposited a thick layer of Au as top electrode, thus the devices do not operate as solar cells, since due to the opaqueness of Au electrode, light penetration and absorption by the perovskite layer are hindered. The configuration of the diode devices we fabricated is illustrated in Fig. 1b.

a) GaAs nanowires

The starting point of the device assembly consists of the preparation and insulation of the substrate and the GaAs NW transport layer. NWs were grown in self-catalyzed Vapor-Liquid-Solid (VLS) mode by Molecular Beam Epitaxy (MBE) on heavily doped (n^+) Si(111) substrates[25,26,27] As for the nanowire growth, Ga droplet was used as self-catalyst instead of a metal (Au) catalyst. Controlled n-type doping of the NWs can be achieved by the growth of an exterior Si-doped GaAs "shell" around the intrinsic GaAs "core"[28] (Fig.1c). The surface density and spatial parameters of the NWs were carefully adjusted in order to provide sufficient unoccupied area on the template for the unobstructed deposition of the perovskite layer. Details can be found in the Experimental Part.

To insulate the perovskite film from the n+ Si substrate (as well as from any GaAs-related structures other than NWs on the substrate), a few hundreds of nanometers layer of the organic polymer Cyclotene 3022-46 benzocyclobutene (BCB) was deposited via spin-coating process in between the array of NWs.

b) Deposition of $CH_3NH_3PbI_3$ perovskite

The deposition of the perovskite was based on spin casting of solution techniques and it was branched in two different approaches: the conventional single-pot solution method where all the reagents were dissolved in a polar solvent (typically dimethyl formamide, DMF)[29] and the so-called "two-step method"[30,31] where the constituent reagent of $CH_3NH_3PbI_3$ (PbI_2 and CH_3NH_3I) were deposited sequentially as separate processes (Fig. 2).

Comparing the two deposition techniques, we find that the two-step method is strongly preferable for this device configuration, not only because it offers a better control of the growth directionality of the perovskite[32], but also because the direct spin-coating approach causes severe damage to the GaAs NWs, often leading to complete "uprooting" of the material from the substrate.

Because of this trend, deposition optimization was focused exclusively on the two-step method, varying the precursor solutions' concentration and the dwelling time of the film in the CH_3NH_3I solution. Specifically, PbI_2 layer is first deposited by spin-coating process, at low revolution rate to prevent NW damage, followed by the reaction with CH_3NH_3I dissolved in a

DOI: 10.54227/mlab.20250005

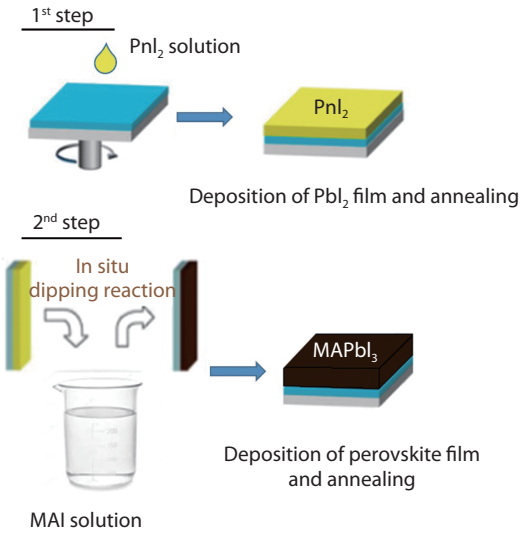

Fig. 2 Schematic representation of the two-step sequential deposition method, that was used for the deposition of perovskite layer.

mix of solvents, a polar alcoholic solvent and a nonpolar solvent via dipping process in a solid/liquid reaction(Fig.3a-b)[33].

For the two-step method, the perovskite film formation hinges between two competing effects: nucleation[34–36] and crystallization[36–38]. Generally, low CH_3NH_3I solution concentrations (≤8 mg/ml) lead to uniform distribution of small crystallites that do not exhibit any preferential growth, but as a drawback they lead to an incomplete conversion to the perovskite, leaving a substantial amount of PbI_2 residue. On the contrary, at high CH_3NH_3I concentrations, dissolution and recrystallization process of perovskite crystals takes place, leading to a complete conversion to the perovskite but produce large rod-shaped crystals that lead to a highly inhomogeneous film. In all these processes, soaking time is a very sensitive tuning parameter, since the interruption of the crystal growth at the opportune moment can also lead to the desired film homogeneity.

In order to fine-tune these processes and produce a uniform perovskite film, evenly distributed between the NWs, a "golden ratio" between the two extremes has to be sought. Our approach involves the replacement of the commonly used solvent 2-propanol with a slightly less polar solvent 1-pentanol, which is beneficial for inhibition of water diffusion into the solution during crystal growth. Addition of the nonpolar solvent *n*-heptane to the mixture further amplifies this effect leading to solution mixtures that can be stable in air for more than 24 h, providing sufficient time for the reaction to complete. In this solvent mixture, the optimal dipping conditions involve dipping of the PbI_2 film (1.1M in DMF) in a 15 mg/ml 1-pentanol-heptane mixture for a total dipping time of 30 min and 60 min, out of which the diode devices were fabricated.

As evidenced from XRD and spectroscopic characterization

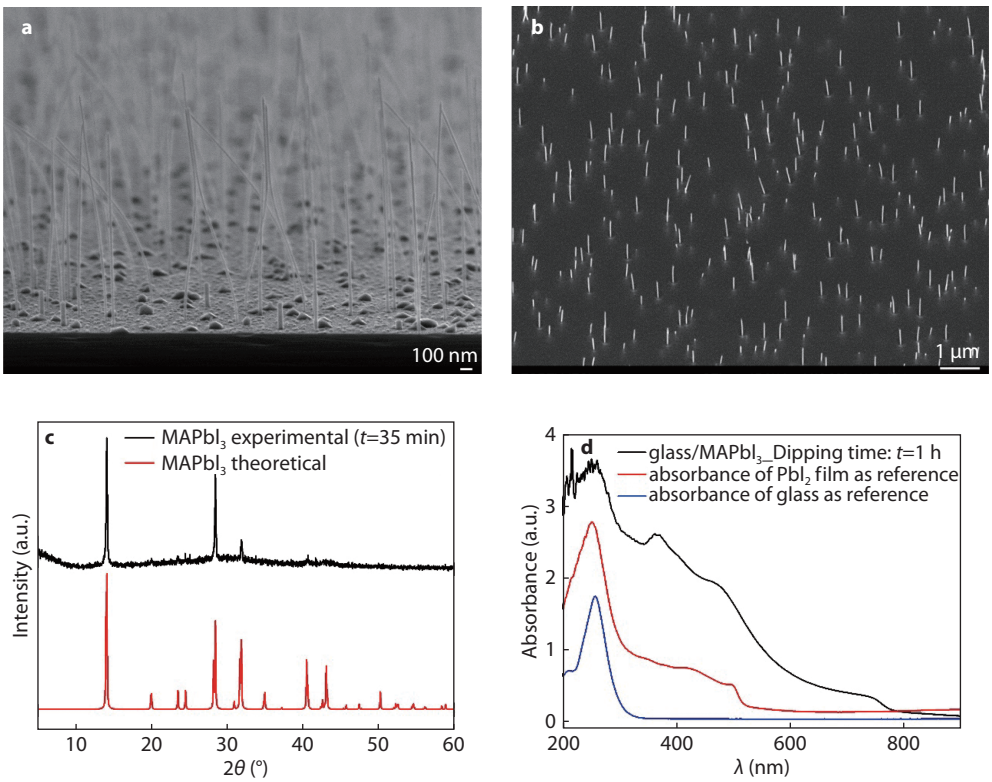

Fig. 3 **a**, **b** SEM images of the as-grown GaAs NWs in cross-plane and near-vertical view, for undoped NW structures (see NW composition in figure 1c), before and after the deposition of BCB layer on nanowire structures, respectively. **c** XRD pattern of the $CH_3NH_3PbI_3$ perovskite film prepared on a glass substrate by the modified two-step sequential deposition method in comparison with the theoretical XRD pattern. Strong preferential orientation of the crystals is observed. **d** Absorption spectrum of the $CH_3NH_3PbI_3$ perovskite film on soda lime glass.

DOI: 10.54227/mlab.20250005

on glass substrates, these conditions provide excellent quality of the perovskite film, as judged by the excellent matching of the X-ray diffraction pattern, validating the chemical purity of the compound, as well as in terms of the optical absorption spectra which are consistent with the expected bandgap of the material (Fig. 3c-d).

Characterization of the heterostructure

c) Morphology and Chemical Integrity

After completing the assembly of the $CH_3NH_3PbI_3$/GaAs NW heterostructure, we have proceeded in assessing the structural integrity of the device. Indeed, as shown in Fig. 4, SEM images reveal a homogeneous blending of the $CH_3NH_3PbI_3$ layer with the GaAs NWs. The rod-shaped perovskite crystallites completely cover the GaAs NWs, with the perovskite crystallites showing a relatively uniform distribution with only a few larger crystals sparsely localized (Fig. 4a). The uniformity of perovskite structure that was achieved lies in the capability to control the crystallization of perovskite crystals by using the modified two-step deposition method, which is based in a different mechanism for the growth of perovskite crystals than conventional two step method. However, by increasing the dipping time to t=1 h (Fig. 5b), pinholes appeared, which can lead to structural inhomogeneity of perovskite layer and have detrimental effect on the deposition of the HTL overlayer and the overall performance of the completed device. Also, in this case perovskite layer fully covers the nanowire structures.

X-Ray Diffraction on the heterostructure (Fig. 4c-d) clearly confirms the presence of the perovskite on the heterostructure, even though it is severely masked by the very strong diffraction originating from the highly-oriented single-crystalline (111) silicon substrate.

Last, the homogeneous deposition of perovskite layer on nanowire structures is also revealed in the cross-section SEM image of the diode device, as seen in Fig. 5. GaAs nanowires are not apparent through the perovskite layer, which is attributed to non-efficient cleaving of the diode device for taking the SEM image in cross-section.

d) Electrical characterization

Upon validating the successful formation of the heterostructure, we proceeded to the completion of the device by depositing the HTL layer (spin-coating) and the top electrode (sputtering). Spiro-OMeTAD was used following the standard protocol. The complete circuit does indeed exhibit diode behavior, thus indicating the successful fabrication of the device (Fig. 6).

The diode characteristics were further evaluated according to a simplified equivalent circuit (Fig. 6a). Based on the fitting parameters of the data, which are tabulated in Table 1, we can conclude that the device for the case of undoped GaAs NWs, suffers from a very high series resistance (R_{series}) and severe recombination losses expressed by an ideality factor (n) that largely deviates from unity[39].

Comparing between the diodes fabricated using different deposition conditions for the perovskite layer and the degree

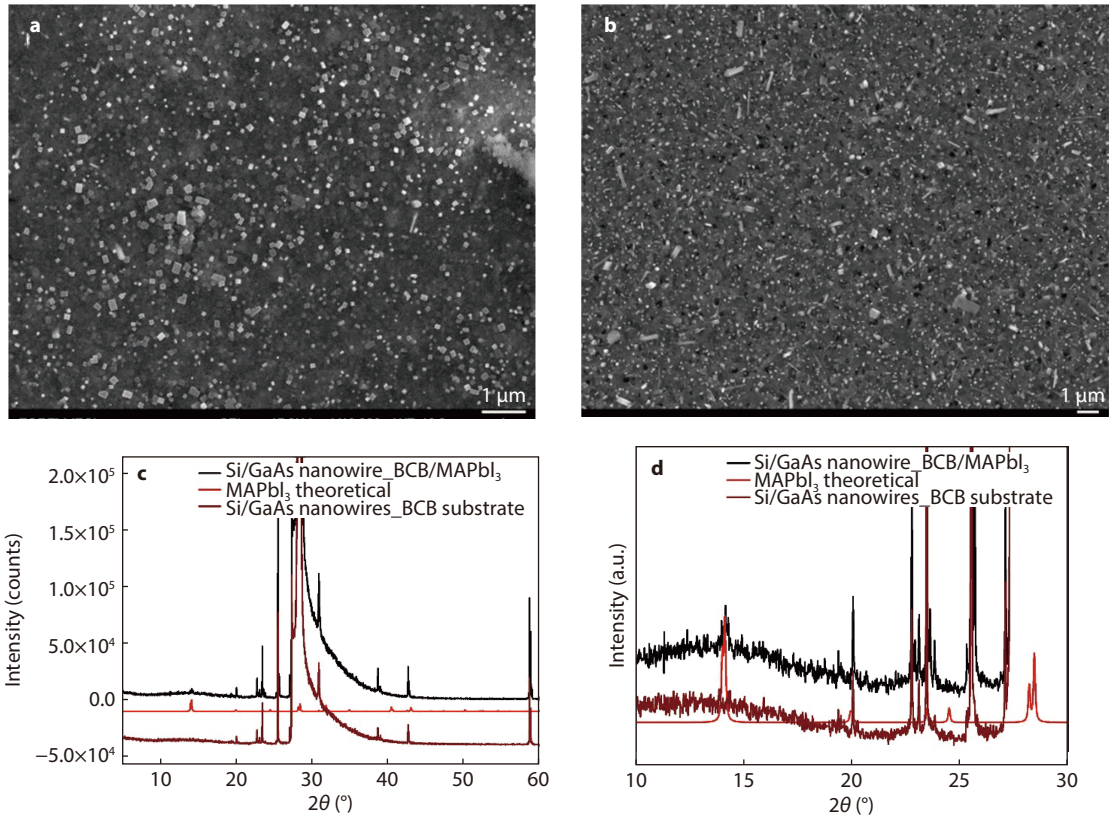

Fig. 4 **a**, **b** SEM images of the $CH_3NH_3PbI_3$/GaAs NW heterostructure for two different perovskite deposition conditions (30 min and 60 min dipping time, respectively). **c**, **d** XRD pattern of the $CH_3NH_3PbI_3$/GaAs NW heterostructure indicating the formation of crystalline perovskite on top of the nanowires, evidenced by the reflection at ~ 14°. The overarching peak at 2θ = 29° results from the (111)-oriented Si substrate.

DOI: 10.54227/mlab.20250005

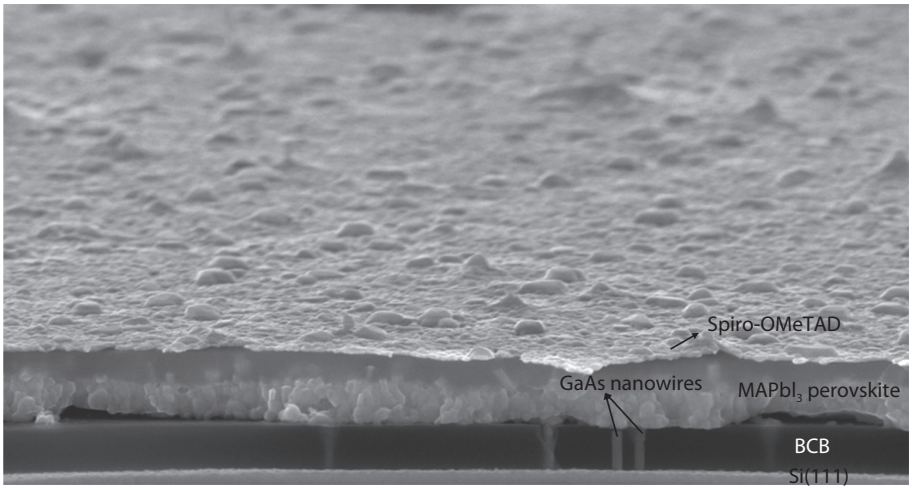

Fig. 5 SEM image in cross-section for the diode device, in case of 1 h dipping time. The (circular) electrode layer is not included in the SEM image. In the SEM image, homogeneous deposition of perovskite layer on nanowire structures is revealed. GaAs nanowires are not apparent through the perovskite layer which is attributed to non-efficient cleaving of the diode device for taking the SEM image in cross-section.

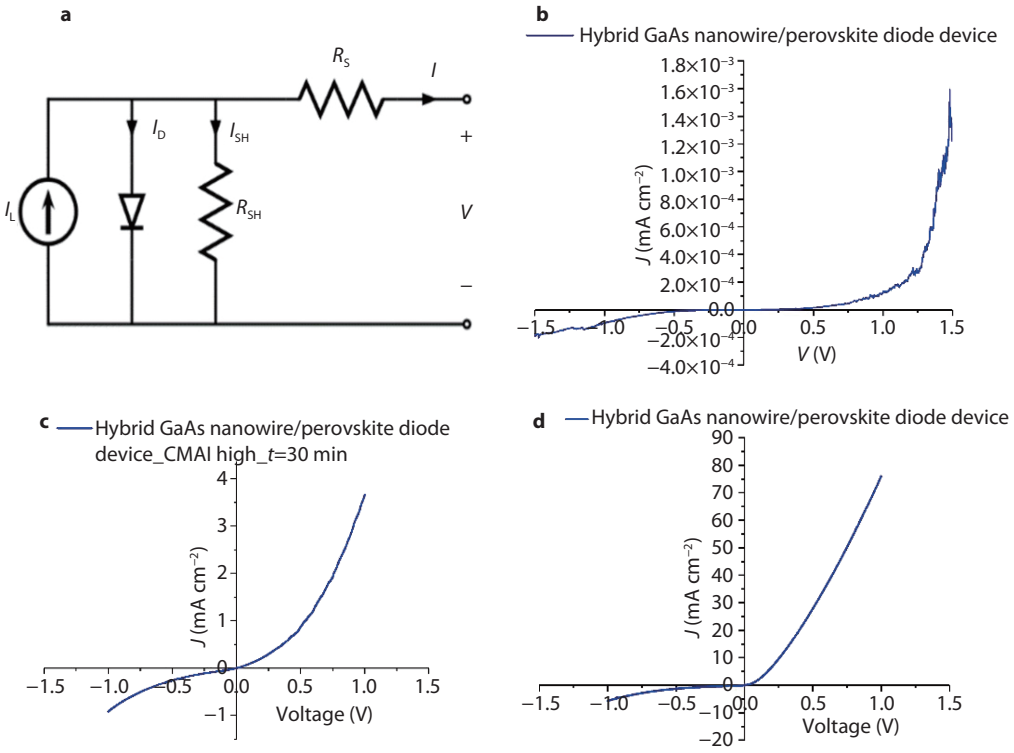

Fig. 6 **a** Schematic representation of the equivalent electrical circuit of the $CH_3NH_3PbI_3$/GaAs NWs heterojunction. **b** I-V characteristics of the diode between pristine GaAs NWs and $CH_3NH_3PbI_3$. **c**, **d** I-V characteristics of the diode between doped GaAs NWs and $CH_3NH_3PbI_3$ for two different perovskite deposition conditions (30 min and 60 min dipping times, respectively).

Table 1. Resistance parameters of the diode devices before and after NW doping. In the second case, the resistance parameters of the diode devices that were fabricated using two different deposition conditions (dipping times) for perovskite layer deposition are mentioned as well.

Deposition conditions	R_{series}	R_{shunt}	A_{diode}	R_s * A_{diode}	R_{sh} * A_{diode}	Ideality factor
Undoped GaAs nanowires	0.12*GΩ	1.7 GΩ	0.0725 cm^2	8.7 MΩ*cm^2	123.25 MΩ*cm^2	4.6
n^+-type doped GaAs shell (Dip. time: t=30 min)	22.54 kΩ	169.5 kΩ	0.00785 cm^2	0.177 kΩ*cm^2	1.33 kΩ*cm^2	1.83
n^+-type doped GaAs shell (Dip. time: t=1 h)	841.87 Ω	11.31 kΩ	0.0095 cm^2	8 Ω*cm^2	107.4 Ω*cm^2	4.5

of doping in the GaAs NWs, we can observe large deviations in the I-V characteristics (Figures 6(b-d) and Table 1). After doping the GaAs NWs, high measurable current was observed, originating from the significantly improved R_{series}, observed for both perovskite deposition conditions. The observed improvement, which spans several orders of mag-

DOI: 10.54227/mlab.20250005

nitude in terms of carrier transport efficiency, indicates, indeed, a better electron transport pathway at the $CH_3NH_3PbI_3$/GaAs NWs interface, resembling much more the schematic band alignment diagram between the two semiconductors. Thus, the effect of GaAs doping on the chosen $CH_3NH_3PbI_3$/GaAs heterointerface architecture is of paramount importance and is associated with the large decrease of the resistivity of the circuit (Table 1), which in turn enables GaAs to operate as an efficient ETL layer, following the conceptual design of the device.

Nevertheless, we observe that shunt resistance is low, in case of doped NWs for both perovskite depositions. The low shunt resistance value is justified considering the growth of perovskite structure. Specifically, for the case of 30 min dipping time, the existence of large size crystals in perovskite structure results in inhomogeneity of perovskite layer. The inhomogeneity of perovskite structure can lead to the formation of trap pathways of carriers at the interfaces of the layers that act as a barrier for carrier transport, creating recombination losses.

On the other hand, for the case of 1 h dipping time, the existence of pinholes in perovskite structure can also generate trap states of carriers that can lead to significant recombination losses. This fact justifies the much lower value of shunt resistance, as compared to the case of 30 min dipping time.

Last, the high value of ideality factor (~4.5 as observed in Table 1） is attributed to recombination losses that are a result of the low value of shunt resistance, which is lower than the optimum reported value for $MAPbI_3$ (~5 kΩ*cm^2)[40].

Even though we fabricated diode devices and not solar cell devices, we managed to extract some indirect photo-diode characteristics of these devices, as shown in Figure S1 of the supplementary section, owing to light absorption in the periphery of the Au contacts. Specifically, supposing that free photo-carriers have a diffusion length of 1 μm, assuming an optimal perovskite performance[41], the maximum distance that they can travel until they reach the electrode is 1 μm. This means that carriers that have to travel longer distances than 1 μm, would recombine before they would be able to reach the electrode (see Figure S1 and the associated discussion). Therefore, we assume that carriers can be collected at a ring region of 1 μm around the Au electrode, that has a circular shape. Thus, taking into account the ring area and the I-V characteristics of the devices under illumination conditions, we assessed a photovoltaic conversion efficiency (PCE) of 0.49%, for the case of doped GaAs NWs and a 30 min dipping time. In addition, it is worth mentioning that we observed open circuit voltage (V_{oc}) values of the devices ranging from 0.05 V to 0.15 V, under illumination conditions. Thus, we infer that despite the opaqueness of the top electrode, a measurable photo-response of the devices was observed, that is encouraging for observing efficient photo-response in the corresponding solar cell device, including transparent Indium Tin Oxide (ITO) as top electrode.

Conclusions

Hybrid GaAs NW/$MAPbI_3$ perovskite diode devices were successfully fabricated and the heterojunction diode response has been thoroughly analyzed. We have identified that the doping level of the GaAs NWs is critical for the performance of the diodes, as indicated by the very low series resistance value. Also relevant in this context is the deposition method of the perovskite, with a modified two-step deposition method producing thus far the most promising results. This fact indicates enhanced electron transport through GaAs NWs, constituting an encouraging result for follow-up demonstration of complete solar cell functionality, using GaAs NW structures, as ETL. However, recombination losses are still present in the diode devices, as indicated by the relatively low values of shunt resistance. Therefore, we suggest that by further optimizing perovskite morphology, eliminating the formation of pinholes in the perovskite layer, shunt resistance would be increased, thus charge transport would be improved. In addition, we observed indirect photo-diode characteristics of the diode devices that we fabricated, which is encouraging for the efficient operation of solar cell devices, including GaAs NWs as ETL. However, addressing the fabrication of GaAs/perovskite solar cells, several obstacles need to be overcome, as an effective way of illuminating the device past the mostly opaque layers of the heterojunction. Possible steps in this direction involve the deposition of ultra-thin (<20 nm), semitransparent Au electrodes and/or the deposition of a Transparent Conductive Oxide (TCO) as an alternative transparent electrode. The present work represents the first step towards an unexplored direction in the field of emerging photovoltaic materials and we anticipate that future experiments will lead to the successful realization of III-V/perovskite semiconductor heterojunction solar cells.

■ ACKNOWLEDGEMENTS

The project “NANO-TANDEM” (MIS 5029191), co-financed by Greece and the European Regional Development Fund. CCS acknowledges the support from the Special Account for Research Funding of the University of Crete (grants KA10330 and KA10652),

Experimental part

Materials. Anhydrous N,N Dimethylformamide (99.8%), Spiro-OMeTAD (99%), 4-tert-Butylpyridine (TBP) (98%) and Bis(trifluoromethane)sulfonamide lithium salt (LITFSI) was purchased from Sigma Aldrich. 1-pentanol (98+%) was purchased from Alfa Aesar. Heptane (>99%) was purchased from Merck. All chemicals were used as received.

GaAs nanowire epitaxial growth. Undoped GaAs NWs (30 nm in diameter) were grown in self-catalyzed Vapor-Liquid-Solid (VLS) mode on n^+ Si(111) substrates by solid source MBE[25,26]. For the realization of n-type doping, the undoped NWs were overgrown by a 35 nm-thick Si-doped GaAs shell (nominal electron concentration: 10^{18} cm^{-3})[27]. This resulted in an average total NW diameter of <d>=100 nm. Both undoped and n^+-type doped GaAs NWs were used for the fabrication of the diode devices. The average NW height is <L>=1 μm (1.2 μm) and the average NW density is <D>=4.8×10^7 cm^{-2} (3×10^8 cm^2) for the doped (undoped) NWs. For completeness, it should be mentioned that the undoped cores of the doped NWs were grown in pulsed mode[26], whereas the undoped NWs in conventional (i.e. continuous) mode[25]. Fur-

DOI: 10.54227/mlab.20250005

thermore, the undoped NWs contain two AlGaAs segments of a few nm close to the NW tip (for a different study). Both aforementioned differences, though, are not expected to have any noticeable effect on the diode characteristics.

Electrical insulation of GaAs. For the devices fabrication, Cyclotene 3022-46 benzocyclobutene (BCB) polymer was deposited on NW template via spin coating technique using the following spinning conditions: i) 300 rpm spinning velocity and 300 rpm s^{-1} acceleration, t=10 sec and ii): 3000 rpm spinning velocity and 300 rpm/s acceleration, t=40 s. Subsequently, BCB is baked at 110 °C for 1 min. Further steps of thermal treatment are followed: iii) A gradual decrease in temperature (ramp) to 20 °C in 2 sec and a stay at this temperature for 2 sec. iv) A ramp to 100 °C in 15 min and a stay at this temperature for 15 min. v) A ramp to 150 °C in 15 min and a stay at this temperature for 15 min. vi) A ramp to 250 °C in 1 h and a stay at this temperature for 1 h. vii) A gradual temperature decrease (ramp) to 20 °C in 30 min and a stay in this temperature for 2 sec. viii) BCB etching with Reactive-Ion Etching (RIE) follows until NWs to emerge in the desired height. The conditions of this process are the following: power is 200 W, pressure is 140 mTorr, and the process time is 11 min. After, BCB etching, the NW height above BCB layer is 500 nm for the doped nanowires and 300 nm for the undoped ones. $MAPbI_3$ perovskite layer was then deposited on Si/GaAs NW-BCB film, as described above.

Substrate cleaning. Si/GaAs NW-BCB substrates were subject to ultrasonicating cleaning according to the following procedure: the substrates were ultra-sonicated in Helmanex water solution (Helmanex/water volume ratio: 2/98) for 15 min at room temperature. They were subsequently rinsed with water and followingly deionized water. Next, the substrates were firstly ultra-sonicated for 15 min in isopropanol and then acetone solvent, at room temperature, as well. Subsequently, they were rinsed with copious amounts of acetone firstly and then isopropanol for further cleaning. Last the substrates were removed from isopropanol solution and immediately dried by blowing with a N_2 piston. After the cleaning preparation, the substrates were submitted to oxygen plasma treatment, using power P=88 mW for 15 min and oxygen gas flow of 50 cm^3/min.

Preparation of precursor powders. PbI_2 and CH_3NH_3I (MAI) powders were prepared in the lab, using the following preparation process:

For MAI powder preparation, equimolar quantities of methylamine (CH_3NH_2) and HI (57% w/w in H_2O) were mixed, followed by evaporation of the solvent at 80 °C under vacuum.

The preparation of PbI_2 powder is implemented by the double exchange reaction between lead nitrate and potassium iodide ($Pb(NO_3)_2$:KI)=1:2. Two aqueous solutions were prepared and, upon mixing, PbI_2 powder was precipitated in nearly quantitative yields. PbI_2 powder was isolated from the solution via suction filtration and drying under vacuum.

Solvent drying. For the preparation of precursor solutions for perovskite layer deposition, we used dried solvents before use. Because 1-pentanol solvent is not anhydrous, we dried it by using molecular sleeves (zeolites). For the drying preparation of 1-pentanol,zeolites were first dried by annealing them in an oven (Eurotherm 2408CP, 2408P4, 2408CM (Carbolite)) at 500 °C, overnight. Subsequently, they were added in hot (pre-heated) 1-pentanol solvent, inside a conical flask and then the flask was immediately capped with a septum cap.

Perovskite film fabrication. For perovskite deposition, two step spin-dipping method was used and specifically non-polar solvent technique[32]. Immediately before PbI_2 and CH_3NH_3I (MAI) solution preparation, both PbI_2 and MAI powders were dried by heating them in a vacuum oven (model: EV 018) at 58 °C under vaccuum overnight. For the deposition process of perovskite layer, firstly PbI_2 solution was prepared (C=1.1 M), by dissolving 405.68 mgr (0.88 mmol) of PbI_2 powder in 0.8 ml of N,N-Dimethylformamide (DMF), at 100 °C, until complete dissolution of the powder is achieved. Then, when the solution is cooled at room temperature, it was filtered using a 0.45 μm pore-size hydrophilic filter. PbI_2 solution is deposited on the clean and oxygen plasma pre-treated substrates (Si/GaAs NW-BCB layer) via spin coating,using the following program of spinning conditions for each deposition: i) 300 rpm, 300 rpm s^{-1}, 10 s and ii) 3000 rpm, 300 rpm/s, 40 s. For the pre-treatment of the substrates using oxygen plasma, the Zepto 119440 (Diener) instrument was used. After the deposition of PbI_2 on the films, PbI_2 films were annealed at 90 °C for 2 min. Next, at the second stage of the fabrication method, MAI solution (dipping solution) was prepared by dissolving MAI (15 mgr ml^{-1}) in a mix of solvents: anhydrous 1-pentanol (98+%) and heptane at (2:1) volume, respectively. Specifically, 90 mgr (0.566 mmol) of MAI were dissolved in the mix of solvents: 6 ml of anhydrous 1-pentanol, 3 ml of heptane. After the annealing stage of PbI_2 films, they were left to cool down, at room temperature, and then they were dipped into the MAI solution. In the solution, in-situ reaction of PbI_2 and MAI reactants takes place, for the formation of $MAPbI_3$ perovskite phase. To ensure complete conversion of PbI_2 to perovskite phase, the films were left in the dipping solution for high dipping time, specifically for 30 min and 1 h. After dipping, the perovskite films were dried by blowing dry nitrogen gas using a N_2 piston to remove residual MAI from the film and they were subsequently annealed on a hotplate at 60 °C in air for 5 min. The $MAPbI_3$ perovskite films (of ~500 nm thickness) were fabricated, in air.

Diode device fabrication.

An ~160 nm, 2,2,7,7′-tetrakis-(N,N-di-p-methoxyphenylamine)9,9′ spirobifluorene (spiro-OMeTAD) layer was subsequently deposited, as the p-type layer of the device. As for the HTL solution preparation, 0.08 gr (65.3 mmol) Spiro-OMeTAD (C=65.3 Mm), 2.7 mgr (9.1 mmol) Bis-(trifluoromethane)sulfonimide lithium salt (LiTFSI) (C=9.1 mM) and 3.5 μl (25 mmol) 4-tert-butylpyridine (tBP) (C=25 mM) were dissolved in 1 ml chlorobenzene. The solution was stirred at room temperature with partially cap open for about 12-16 h, so as to be oxidized in air. The color of the solution should be orange or pink. Then the solution was infiltrated using a 0.45 μm pores-size filters. Spiro-OMeTAD was deposited on the film via spin-coating technique, using the following spinning conditions: 4000 rpm, 1000 rpm/s, 30 s. Subsequently, the films were dried under vacuum for 30 min. Next, Au layer was deposited (thickness:110 nm) via dc magnetron sputtering technique, using MED 020 Sputter coater. A shadow mask was depos-

DOI: 10.54227/mlab.20250005

ited on the samples before the sputtering process, for selective coating of the sample with Au metal. So, Au was deposited in the form of circular spots that had a diode area: A_{diode}=0.00785 cm^2. The deposition conditions of Au layer were: pressure P=3*10^{-2} mbar, current I=30 mA, operation voltage V=333 V, Au deposition rate is 0.59 nm/s. The devices fabrication was performed at ambient conditions.

Device morphology

For the study of perovskite and nanowire heterostructures, a high resolution Scannning Electron Microscope FE-SEM, JEOL JSM-7000F was used, equipped with INCA microanalysis system (Oxford Instruments). The microscope is equipped with Schottky type field-emission (T-FE) gun with a Zr/O Tungsten emitter. Images were collected at 15 kV accelerating voltage.

X-Ray diffraction (XRD) characterization

For the study of crystal quality of perovskite structure, a Bruker D8 ADVANCE XRD system was used, employing a Cu source, with Cu Kα1 radiation (λ=1.5406 Å) operating at 40 kV and 40 mA. For the XRD measurements, the 2 theta angles range was 2°-60° and the rate of measurements was 0.02°/sec.

Optical characterization

1 Photoluminescence (PL) measurements

Photoluminescence measurements were carried out at room temperature. The excitation was performed using a cw He-Cd laser with λ = 325 nm, with laser power 2 mW. The spectra were obtained using spectrometer with grating 150 groove/mm and a very sensitive LN_2-cooled CCD.

2 UV-vis -NIR measurements

The absorption, reflection, and transmission measurements were performed in a Shimadzu UV-2600 spectrophotometer, equipped with an ISR-2600 Plus two-detector integrating sphere, enabling measurements in the 185 nm-1400 nm wavelength region.

Electrical characterization of the devices.

For the electrical characterization of the devices, the current density versus voltage (J–V) data were collected in air without any encapsulation using a Keithley 2400 source meter, operating both as a voltage source and current meter.

■ REFERENCES

1. H. Min, D. Y. Lee, J. Kim, G. Kim, K. S. Lee, J. Kim, M. J. Paik, Y. K. Kim, K. S. Kim, M. G. Kim, T. J. Shin, S. Il Seok, *Nature*, 2021, 598, 444
2. A. D. Taylor, Q. Sun, K. P. Goetz, Q. An, T. Schramm, Y. Hofstetter, M. Litterst, F. Paulus, Y. Vaynzof, *Nat. Commun.*, 2021, 12, 1878
3. M. Saliba, T. Matsui, J. -Y. Seo, K. Domanski, J. -P. Correa-Baena, M. K. Nazeeruddin, S. M. Zakeeruddin, W. Tress, A. Abate, A. Hagfeldt, M. Grätzel, *Energy Environ. Sci.*, 2016, 9, 1989
4. M. Lyu, S. Park, H. Lee, B. S. Ma, S. H. Park, K. -H. Hong, H. Kim, T. -S. Kim, J. H. Noh, H. J. Son, N. -G. Park, *ACS Appl. Mater. Interf.*, 2021, 13, 35595
5. National Renewable Energy Laboratory, Photovoltaic Research. https://www.nrel.gov/pv/cell-efficiency , July 2024.
6. Z. Li, T. H. Kim, S. Y. Han, Y. -J. Yun, S. Jeong, B. Jo, S. A. Ok, W. Yim, S. H. Lee, K. Kim, S. Moon, J. -Y. Park, T. K. Ahn, H. Shin, J. Lee, H. J. Park, *Adv. Energy Mater.*, 2020, 10, 1903085
7. J. Wang, P. Zhao, Y. Hu, Z. Lin, J. Su, J. Zhang, J. Chang, Y. Hao, *Solar RRL*, 2021, 5, 2100121
8. J. O. Akinlami, A. O. Ashamu, *J. Semicond.*, 2013, 34, 03200
9. Y. Sun, L. Liu, Z. Lv, X. Zhangyang, F. Lu, and J. Tian, *Mater. Sci. Semicond. Proc.*, 2021, 122, 105498
10. J. He, Y. Shen, B. Li, X. Xiang, S. Li, X. Fang, H. Xiao, X. Zu, L. Qiao, *Opt. Mater*, 2021, 111, 110611
11. A. I. Ayzenshtat, D. L. Budnitsky, O. B. Koretskaya, L. S. Okaevich, V. A. Novikov, A. I. Potapov, O. P. Tolbanov, A. V. Tyazhev, A. P. Vorobiev, *Nucl. Instr. Meth. Phys. Res. Sect. A Accel. Spectrometers, Detect. Assoc. Equip.*, 2002, 494, 120
12. L. Tsakalakos, *Mater. Sci. Eng. R. Rep.*, 2008, 62, 175
13. C. Ghosh, S. Pal, B. Goswami, P. Sarkar, *J. Phys. Chem. C*, 2007, 111, 12284
14. K. Peng, Y. Xu, Y. Wu, Y. Yan, S. T. Lee, J. Zhu, *Small*, 2005, 1, 1062
15. E. Garnett, P. Yang, *Nano Lett.*, 2010, 10, 1082
16. M. D. Kelzenberg, S. W. Boettcher, J. A. Petykiewicz, D. B. Turner-Evans, M. C. Putnam, E. L. Warren, J. M. Spurgeon, R. M. Briggs, N. S. Lewis, H. A. Atwater, *Nat. Mater*, 2010, 9, 239
17. H. Lu and C. Gang, *Nano Lett.*, 2007, 7, 3249
18. C. Lin, M. L. Povinelli, *Appl. Phys. Lett.*, 2010, 97, 071110
19. O. L. Muskens, J. G. Rivas, R. E. Algra, E. P. A. M. Bakkers, and A. Lagendijk, *Nano Lett.*, 2008, 8, 2638
20. S. Fan, J. D. Joannopoulos, *Phys. Rev. B*, 2002, 65, 235112
21. S. G. Tikhodeev, A. L. Yablonskii, E. A. Muljarov, N. A. Gippius, T. Ishihara, *Phys. Rev. B*, 2002, 66, 451021
22. T. Prasad, V. L. Colvin, and D. M. Mittleman, *J. Opt. Soc. Am. B*, 2008, 25, 633
23. S. M. Sze, Semiconductor Devices Physics and Technology, Wiley, New York, 1985
24. T. Bak, M. K. Nowotny, L. R. Sheppard, J. Nowotny, *J. Phys. Chem. C*, 2008, 112, 12981
25. T. Tauchnitz, T. Nurmamytov, R. Hübner, M. Engler, S. Facsko, H. Schneider, M. Helm, E. Dimakis, *Cryst. Growth Des.*, 2017, 17, 5276
26. L. Balaghi, T. Tauchnitz, R. Hübner, L. Bischoff, H. Schneider, M. Helm, E. Dimakis, *Nano Lett.*, 2016, 16, 4032
27. H. Choi, Semiconductor Nanostructures for Optoelectronic Devices: Processing, Characterization and Applications, Springer Verlag, Berlin, 2012
28. E. Dimakis, M. Ramsteiner, A. Tahraoui, H. Riechert, L. Geelhaar, *Nano Res.*, 2012, 5, 796
29. Z. Yang, S. Zhang, L. Li, W. Chen, *J. Mater.*, 2017, 3, 231
30. K. Liang, D. B. Mitzi, and M. T. Prikas, *Chem. Mater*, 1998, 10, 403
31. J. Burschka, N. Pellet, S.-J. Moon, R. Humphry-Baker, P. Gao, M. K. Nazeeruddin, M. Grätzel, *Nature*, 2013, 499, 316
32. D. H. Cao, C. C. Stoumpos, C. D. Malliakas, M. J. Katz, O. K. Farha, J. T. Hupp, M. G. Kanatzidis, *APL Mater*, 2014, 2, 091101
33. H. N. Chen, Z. H. Wei, H. X. He, X. L. Zheng, K. S. Wong, and S. H. Yang, *Adv. Energy Mater.*, 2016, 6, 1502087
34. M. Abbas, L. Zeng, M. R. Fei Guo, X.-C. Yuan, and B. Cai, *Materials*, 2020, 13, 4851
35. W. A. Dunlap-Shohl, Y. Zhou, N. P. Padture, and D. B. Mitzi, *Chem. Rev.*, 2019, 119, 3193
36. L. Ke and L. Ding, "Perovskite crystallization", *J. Semicond.*, 2021, 42, 080203,
37. S. C. Watthage, Z. Song, G. K. Liyanage, A. B. Phillips, M. J. Heben, *2016 IEEE 43rd Photovolt. Spec. Conf.*, 2016, 2, 0831
38. W. Kong, G. Wang, J. Zheng, H. Hu, H. Chen, Y. Li, M. Hu, X. Zhou, C. Liu, B. N. Chandrashekar, A. Amini, J. Wang, B. Xu, C. Cheng,

DOI: 10.54227/mlab.20250005

Solar RRL, 2018, 2, 1700214
39. P. Singh and N. M. Ravindra, *Emerg. Mater. Res.*, 2012, 1, 33
40. P. J. Lakshmi, E. Goel, A. Kumar, *Opt. Quant. Electron.*, 2023, 55, 610
41. S. D. Stranks, G. E. Eperon, G. Grancini, C. Menelaou, M. J. P. Alcocer, T. Leijtens, L. M. Herz, A. Petrozza, H. J. Snaith, *Science*, 2013, 342, 341